RESEARCH ARTICLE

NANOPHOTONICS

Negative refraction in hyperbolic hetero-bicrystals

A. J. Sternbach[1]*, S. L. Moore[1], A. Rikhter[2], S. Zhang[1], R. Jing[1], Y. Shao[1], B. S. Y. Kim[3], S. Xu[1], S. Liu[3,4], J. H. Edgar[4], A. Rubio[5,6], C. Dean[1], J. Hone[3], M. M. Fogler[2], D. N. Basov[1]

We visualized negative refraction of phonon polaritons, which occurs at the interface between two natural crystals. The polaritons—hybrids of infrared photons and lattice vibrations—form collimated rays that display negative refraction when passing through a planar interface between the two hyperbolic van der Waals materials: molybdenum oxide (MoO_3) and isotopically pure hexagonal boron nitride ($h^{11}BN$). At a special frequency ω_0, these rays can circulate along closed diamond-shaped trajectories. We have shown that polariton eigenmodes display regions of both positive and negative dispersion interrupted by multiple gaps that result from polaritonic-level repulsion and strong coupling.

Refraction is an elemental phenomenon in optics, in which a ray of light changes direction after traveling across an interface between two media (*1*). Refraction is considered "negative" if the refracted beam emerges on the same side of the interface normal as the incident one. This uncommon occurrence was demonstrated in artificial metamaterials (*2*) and superlattices (*3*) whose permittivity ε and permeability μ are simultaneously negative. Negative refraction alters light amplification and emission (*4*, *5*) as well as nonlinear optics (*6*) and may also cause trapped light (*7*, *8*) as well as "perfect" lensing (*9*). Interfaces between anisotropic meta-structures with rotationally misaligned principal axes can also enable negative refraction (*10*–*12*). Extreme anisotropy is offered by hyperbolic materials (HMs), whose hybrid light-matter modes—polaritons—are predicted to exhibit all-angle negative refraction at carefully crafted interfaces (*11*, *13*). In this work, we studied polaritons in a previously unexplored class of hyperbolic hetero-bicrystals made of two thin crystals, molybdenum oxide (MoO_3) (*14*–*18*) and isotopically pure hexagonal boron nitride ($h^{11}BN$) (*19*–*21*). Our hyperspectral nano-imaging data reveal localization, negative refraction, and closed-loop circulation of polaritonic rays inside $h^{11}BN$-MoO_3 hetero-bicrystals. Central to the observed effects is the gap in the polaritonic dispersion, which we extracted from hyperspectral images of polaritonic waves.

The hyperbolic electrodynamics of both $h^{11}BN$ (crystal A) and MoO_3 (crystal B) is born out of strong dipole active phonons (*22*). These resonances drive the permittivity negative along at least one principal axis, whereas positive "dielectric-like" positive permittivity is preserved along the remaining principal direction(s). Our results can be understood by focusing on the x-z plane (Fig. 1) for frequencies at which the phonon (Reststrahlen) bands of the constituent crystals overlap, $740\ \mathrm{cm}^{-1} < \omega < 822\ \mathrm{cm}^{-1}$. At these frequencies, the permittivity of $h^{11}BN$ is positive along $\hat{x}$ and negative along $\hat{z}$, $\varepsilon_A^x(\omega) > 0$, and $\varepsilon_A^z(\omega) < 0$ (type-I hyperbolicity). In MoO_3, the signs are reversed, $\varepsilon_B^x(\omega) < 0$ and $\varepsilon_B^z(\omega) > 0$ (type-II hyperbolicity) (Fig. 1A) in the same frequency range.

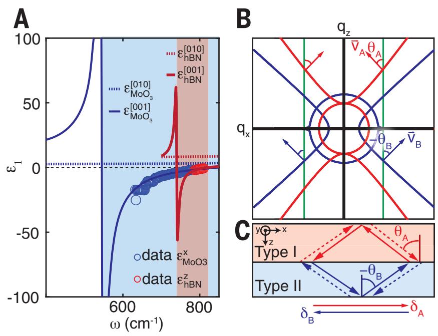

Fig. 1. Polaritons in hyperbolic hetero-bicrystals. (**A**) Real components of the permittivity, ε_1, of $h^{11}BN$ and MoO_3. The dots are experimental data. The parameters for the calculations, indicated with solid lines, are extracted from our data (table S1). (**B**) Schematic showing $q_y = 0$ cuts of the polariton isofrequency surfaces of type-I (crystal A, red) and type-II (crystal B, blue) HMs (supplementary text, section S1). The group velocities $\vec{v}_{A,B}$ and their tilt angles $\theta_A > 0$, $\theta_B < 0$ are indicated. (**C**) Schematic of the polariton rays in a bicrystal assembled from a type-I HM (crystal A, $h^{11}BN$) and a type-II HM (crystal B, MoO_3). The lateral shifts inside the crystals $\delta_A > 0$, $\delta_B < 0$ are indicated with arrows. The ray paths are closed if $\delta_A + \delta_B = 0$.

It is customary to refer to electromagnetic modes of polar materials as polaritons. The polariton dispersion assumes a simple form $(q_x^2/\varepsilon^z) + (q_z^2/\varepsilon^x) = \omega^2/c^2$ when the polariton momentum $\vec{q} = (q_x, q_y, q_z)$ is in the x-z plane, $q_y = 0$. In HMs, the polariton isofrequency lines are hyperbolas (Fig. 1B) (*14*, *19*, *20*, *23*). The asymptotes of these hyperbolas are inclined by the angle ±θ with respect to the x axis, where $\theta = \theta(\omega)$, defined by $\tan\theta = i\sqrt{\varepsilon^x}/\sqrt{\varepsilon^z}$, is positive for type-I and negative for type-II HMs. In the high-q limit, probed in our near-field experiments, the polariton group velocity $\vec{v} = \nabla_{\vec{q}}\omega$ becomes orthogonal to $\vec{q}$ (*24*). Because the angles $\theta_A > 0$ and $\theta_B < 0$ have opposite signs while momentum q_x is conserved, the tangential velocity $v_x = -|v|\,\mathrm{sgn}\, q_x \sin\theta$ changes sign in refraction at the A-B interface. The net effect is that polaritons exhibit negative refraction (supplementary text, section S1).

We report on a new class of hyperbolic hetero-bicrystal structures that reveal negative refraction of polaritons. If a hyperbolic ray emerges on the B-side of the A-B interface, the ray will be laterally displaced by a distance $\delta_B/2 < 0$ after propagating through crystal B. Negative refraction occurs at the interface with crystal A, prompting an additional displacement $\delta_A/2 > 0$. At a frequency ω_0, at which the condition $\delta_A(\omega_0) + \delta_B(\omega_0) = 0$ is satisfied, the polaritons travel in closed trajectories (Fig. 1C, ray construction). Experimental signatures of the closed-cycle electrodynamics near ω_0 are evident in our data (Figs. 2 and 3). However, these observations cannot be explained by polaritonic ray optics alone. We have shown that the principal modes of crystals A and B hybridize into a single strongly coupled eigenmode at ω_0, leading to prominent gaps in frequency-momentum dispersion.

To visualize polaritons, we used scanning near-field optical microscopy (SNOM). In SNOM measurements, the metalized tip of an atomic force microscope probes optical effects with subdiffractional spatial resolution, roughly given by the tip's radius, which is about 20 nm (*25*). To meet the demand for quasi-monochromatic excitation at frequencies within the overlapping Reststrahlen bands of $h^{11}BN$ and MoO_3 (Fig. 1A) (*26*), we generated ultranarrowband mid-infrared pulses with the spectral bandwidth <4 cm^{-1} (supplementary text, section S2.5).

Nano-imaging data unequivocally demonstrated negative refraction in $h^{11}BN$-MoO_3 hetero-bicrystals (Fig. 2). We patterned a gold strip with a width of $2w \approx 750$ nm on the surface of silicon dioxide (SiO_2). The sharp edges of the strip along the y axis enhance the infrared field and excite polaritons in the bicrystal with $q_y \approx 0$ (*27*). A MoO_3 crystal was placed on top of the launcher with its c axis perpendicular to the strip (fig. S7). We obtained images of the scattering amplitude, $|s|$, at temperature

[1]Department of Physics, Columbia University, New York, NY, USA. [2]Department of Physics, University of California San Diego, San Diego, CA, USA. [3]Department of Mechanical Engineering, Columbia University, New York, NY, USA. [4]Tim Taylor Department of Chemical Engineering, Kansas State University, Manhattan, KS, USA. [5]Center for Computational Quantum Physics (CCQ), Flatiron Institute, New York, NY, USA. [6]Max Planck Institute for the Structure and Dynamics of Matter, Luruper Chaussee, Hamburg, Germany.
*Corresponding author. Email: as5049@columbia.edu

T = 99 K to minimize losses. Images of $|s|$, collected at the surface of MoO_3 (Fig. 2B), reveal a pair of characteristic twin-peak profiles near the edges of the launching strip (Fig. 2C, inset; marked 1, 2, 3, and 4). The separation, δ_B, between peaks 1 and 2, or equivalently 3 and 4, is consistent with the directional propagation of hyperbolic rays introduced in Fig. 1 (*14*). Further, the magnitude of δ_B increases as the infrared frequency decreases (fig. S8), which also supports the notion of conical ray propagation in MoO_3 that is characteristic for a hyperbolic medium.

Next, we placed a crystal of $h^{11}BN$ on top of the MoO_3-Au (gold) assembly and visualized the nano-optical intensity at the top of the hetero-bicrystal. We observed a single peak of $|s|$ in relation to each edge of the Au strip at ω_0 = 787 cm^{-1} (Fig. 2, A and C). We also detected a considerable intensity between the two peaks (supplementary text, sections S1 and S2.6). Our observations, augmented with modeling, are consistent with negative refraction guiding the hyperbolic rays to the same lateral positions at the top and bottom surfaces of the bicrystal (Fig. 2C, top inset). Effectively, negative refraction delivers a projection of

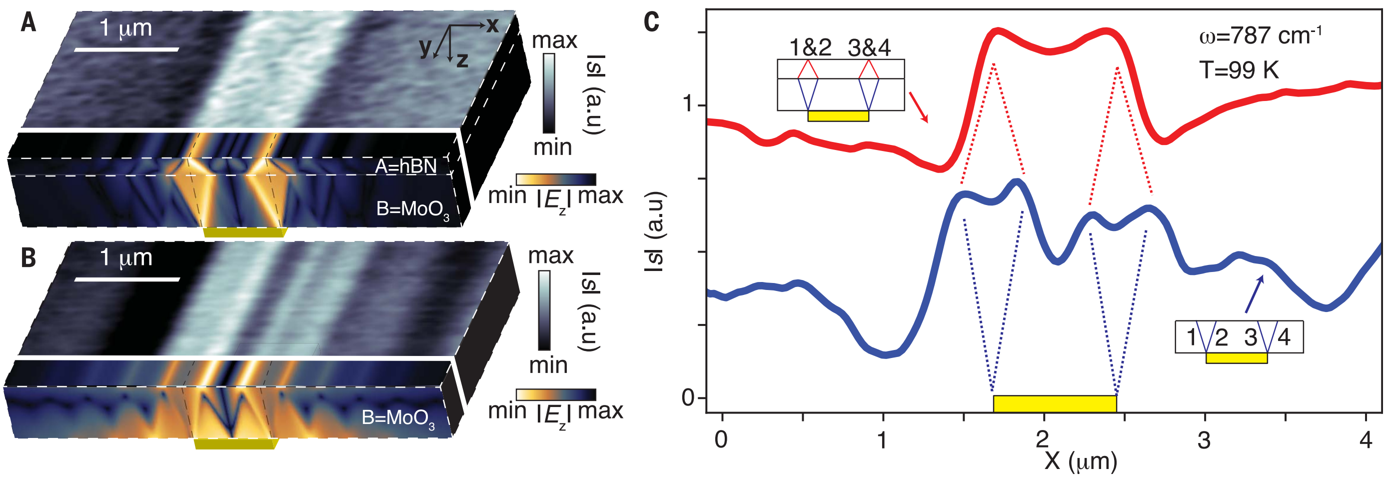

Fig. 2. Negative refraction of polaritons. Near-field amplitude data, $|s|$, obtained at various surfaces in the x-y plane of an $h^{11}BN$-MoO_3-Au stack. All data were obtained with ω = 787 cm^{-1} at temperature T = 99K, with thicknesses d_{hBN} = 98 nm on d_{MoO3} = 290 nm A = $h^{11}BN$ and B = MoO_3 crystals, respectively. (**A**) Imaging data of $|s|$ in perspective at the top surface of $h^{11}BN$-MoO_3-Au. (**B**) Data obtained at the surface of MoO_3-Au, displayed in an identical manner to that of (A). Calculations of $|E_z|$ in the x-z plane, and a strip in the x-y plane, are also shown in false color (supplementary text, section S1) in (A) and (B). Yellow rectangles indicate gold bars, beneath the HMs, and black dashed lines indicate the strip's edges. (**C**) Line profiles of $|s|$ as a function of the real-space coordinate, X. (Insets) The geometry in the x-z plane. Two pairs of hyperbolic rays—1 and 2, and 3 and 4—launched by the two edges of the Au strip are labeled.

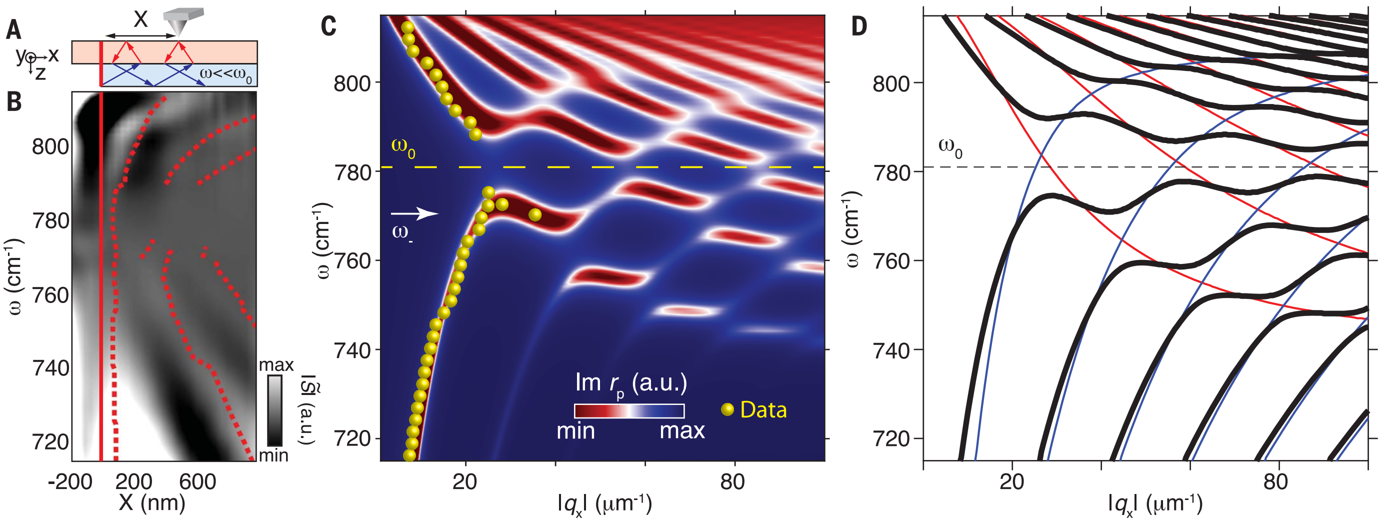

Fig. 3. Spectral gaps in the hetero-bicrystal dispersion. All data were obtained on a $h^{11}BN$-MoO_3 bicrystal with thicknesses of d_{hBN} = 58 nm and d_{MoO3} = 150 nm at ambient temperature. (**A**) Schematic illustrating ray trajectories in $h^{11}BN$ (red) and MoO_3 (blue) for $\omega \gg \omega_0$. (**B**) Amplitude data, $|\tilde{S}(X,\omega)|$ as a function of the distance X between the tip and bicrystal edge (solid red line). The edge of $h^{11}BN$ is located at X = −700 nm (supplementary text, section S1). The red dashed lines indicate locations where maxima are observed in our calculations (fig. S6D). (**C**) The imaginary part of the p-polarized reflection coefficient (Im r_p) is shown as a function of ω and the absolute value of the momentum component, $|q_x|$. The calculation uses realistic room-temperature losses of $h^{11}BN$ and MoO_3 (table S1). Data points are indicated with yellow dots (fig. S6). (**D**) The bicrystal dispersion is indicated with black lines for the idealized case with vanishing losses. Thin color traces indicate the dispersions of the parent crystals, MoO_3 (blue), and $h^{11}BN$ (red) calculated by using parameters in table S1.

the Au strip to the top surface of the bicrystal through diverging and converging trajectories of the hyperbolic rays inside the bicrystal. Numerical simulations capture gross features of the data in Fig. 2, A and B (analysis of subtle differences between the model and experiments is provided in the supplementary text, section S1.3). The totality of data in Fig. 2 and fig. S8 establishes negative refraction at the $h^{11}BN$-MoO_3 interface.

We then inquired into the frequency-momentum (ω, q_x) dispersion of the hetero-bicrystal polaritons and its implications for the observed negative refraction. We collected hyperspectral data of the frequency-dependent near-field amplitude $|\tilde{S}(X,\omega)|$ as a function of the distance X from the bicrystal edge, following established procedures (*20*, *25*, *28*). Except for a narrow window of frequencies around ω_0 = 787 cm^{-1}, we witnessed oscillations (or fringes) of $|\tilde{S}(X,\omega)|$ in our hyperspectral data (Fig. 3B). The period of the oscillations identified in Fig. 3B systematically varies with ω. Thus, our observations revealed how the wavelength of polaritonic waves, $\lambda_p(\omega)$, evolves with the frequency of incident infrared light. The data in Fig. 3B provide access to the polaritonic $(\omega, |q_x|)$ dispersion because $\lambda_p(\omega) = 2\pi/|q_x(\omega)|$ (Fig. 3C). We stress a nonmonotonic trend of $\lambda_p(\omega)$. Indeed, $\lambda_p(\omega)$ decreased when the frequency was near the lower bound of the overlapping Reststrahlen bands, but then reversed the trend near the upper bound of this frequency range. Near the frequency ω_- = 773 cm^{-1}, we detected two different fringe periods; hence, there are two sets of q_x points in the vicinity of ω_- in Fig. 3C (fig. S6). These features, at ω_0 and ω_-, are not present in the dispersions of constituent crystals (fig. S11). Thus, the hyperspectral data in Fig. 3 indicate that polaritons in the bicrystal are coupled modes.

A standard method for calculating the polariton dispersion involves finding the maxima of the reflection coefficient $r_p = r_p(\omega, |q_x|)$ of a p-polarized plane wave (*20*, *28*–*30*). The results for the imaginary part of the p-polarized reflection coefficient (Im r_p) (Fig. 3) reveal the existence of multiple dispersion branches. The data points match the calculated branches with the smallest q_x, the so-called principal modes. The full dispersion of the bicrystal displays a nonmonotonic $|q_x(\omega)|$ punctuated by spectral gaps (Fig. 3C). This dispersion can be understood as the family of avoided crossings exhibited by the modes of the constituent crystals. The polariton branches shown in Fig. 3D have a negative dispersion in crystal A (Fig. 3D, red curves) and positive dispersion in crystal B (Fig. 3D, blue curves) (fig. S11). Accordingly, the dispersion of the coupled modes of the bicrystal alternates in sign each time $|q_x|$ passes through an avoided crossing. The locations of the crossings are determined by a Bohr-Sommerfeld–like quantization condition

$$(\delta_A + \delta_B)q_x = \pi n + \text{const} \tag{1}$$

where n is an integer. Equation 1 implies that the frequency ω_0, at which $\delta_A + \delta_B$ vanishes, is typically gapped at all q_x, which is in agreement with Fig. 3C. Our modeling predicts that the magnitude of these gaps scales with the polariton's velocity. Therefore, the gap decreases as ~$1/|q_x|$, at large $|q_x|$ (supplementary text, section S1). Within the gaps, the pole of $r_p(\omega, q_x)$ occurs at a complex q_x with a nonzero imaginary part even in the absence of dissipation. Thus, exactly at ω_0 the polaritonic modes are evanescent—exponentially localized near a launcher because of the combined effects of negative refraction and wave interference. We observed a gap near ω_0 (Fig. 3C) situated near $|q_x| = 24$ μm^{-1} with the size $\Delta\omega$ = 13 ± 3 cm^{-1}, which is in good agreement with the calculated value of $\Delta\omega(|q_x| = 26\,\mu\text{m}^{-1}) = 16$ cm^{-1} (Fig. 3, C and D). The hetero-bicrystal polaritons visualized here comply with the definition of the strong mode coupling: The magnitude of the gap exceeds the linewidth of the mode (supplementary text, section S1).

In this work, we introduced hyperbolic hetero-bicrystal polaritons. We showed that the interface polaritons in $h^{11}BN$-MoO_3 can display negative refraction, spectral gaps, strong coupling, and localization. These attributes of hetero-bicrystals are broadly relevant to photonic applications (*31*, *32*) by using HMs. Moreover, polaritons in hetero-bicrystals can be focused to subdiffraction-limited spot sizes (*18*, *33*, *34*), which can enable perfect lensing by means of negative refraction (*9*). The attainable focal spots can, however, be limited by extrinsic factors, including crystal losses and imperfect polaritonic launchers (fig. S15). Further, similar to Fabry-Pérot cavities, negative refraction can cause radiation to propagate in closed cycles in our hetero-bicrystal nanocavities. Dielectric losses remain a challenge but could possibly be mitigated with active loss compensation (*4*, *5*, *35*).

REFERENCES AND NOTES

1. N. Yu *et al.*, *Science* **334**, 333–337 (2011).
2. R. A. Shelby, D. R. Smith, S. Schultz, *Science* **292**, 77–79 (2001).
3. A. Pimenov, A. Loidl, P. Przyslupski, B. Dabrowski, *Phys. Rev. Lett.* **95**, 247009 (2005).
4. S. Xiao *et al.*, *Nature* **466**, 735–738 (2010).
5. T. Pickering, J. M. Hamm, A. F. Page, S. Wuestner, O. Hess, *Nat. Commun.* **5**, 4972 (2014).
6. A. K. Popov, V. M. Shalaev, *Opt. Lett.* **31**, 2169–2171 (2006).
7. K. L. Tsakmakidis, A. D. Boardman, O. Hess, *Nature* **450**, 397–401 (2007).
8. K. L. Tsakmakidis, O. Hess, R. W. Boyd, X. Zhang, *Science* **358**, eaan5196 (2017).
9. J. B. Pendry, *Phys. Rev. Lett.* **85**, 3966–3969 (2000).
10. Y. Zhang, B. Fluegel, A. Mascarenhas, *Phys. Rev. Lett.* **91**, 157404 (2003).
11. X. Lin *et al.*, *Proc. Natl. Acad. Sci. U.S.A.* **114**, 6717–6721 (2017).
12. A. J. Hoffman *et al.*, *Nat. Mater.* **6**, 946–950 (2007).
13. J. Jiang, X. Lin, B. Zhang, *Research* **2018**, 2532819 (2018).
14. W. Ma *et al.*, *Nature* **562**, 557–562 (2018).
15. G. Álvarez-Pérez *et al.*, *Sci. Adv.* **8**, eabp8486 (2022).
16. G. Hu *et al.*, *Nature* **582**, 209–213 (2020).
17. M. Chen *et al.*, *Nat. Mater.* **19**, 1307–1311 (2020).
18. J. Duan *et al.*, *Nat. Commun.* **12**, 4325 (2021).
19. A. J. Giles *et al.*, *Nat. Mater.* **17**, 134–139 (2018).
20. S. Dai *et al.*, *Science* **343**, 1125–1129 (2014).
21. H. Herzig Sheinfux *et al.*, Multimodal interference and bound in the continuum modes in indirectly-patterned hyperbolic cavities. arXiv:2202.08611 [physics.optics] (2022).
22. Q. Zhang *et al.*, *Nature* **597**, 187–195 (2021).
23. Z. Jacob *et al.*, *Appl. Phys. B* **100**, 215–218 (2010).
24. R. K. Fisher, R. W. Gould, *Phys. Rev. Lett.* **22**, 1093–1095 (1969).
25. Materials and methods are available as supplementary materials.
26. A. J. Sternbach *et al.*, *Nat. Commun.* **11**, 3567 (2020).
27. P. Li *et al.*, *Nat. Commun.* **6**, 7507 (2015).
28. E. Yoxall *et al.*, *Nat. Photonics* **9**, 674–678 (2015).
29. T. Low *et al.*, *Nat. Mater.* **16**, 182–194 (2017).
30. H. N. S. Krishnamoorthy, Z. Jacob, E. Narimanov, I. Kretzschmar, V. M. Menon, *Science* **336**, 205–209 (2012).
31. G. Lu *et al.*, *Nano Lett.* **21**, 1831–1838 (2021).
32. A. Yariv, *IEEE J. Quantum Electron.* **9**, 919–933 (1973).
33. Z. Zheng *et al.*, *Adv. Mater.* **34**, e2104164 (2022).
34. Q. Chen *et al.*, *Photon. Res.* **9**, 1540–1549 (2021).
35. S. Wuestner, A. Pusch, K. L. Tsakmakidis, J. M. Hamm, O. Hess, *Phys. Rev. Lett.* **105**, 127401 (2010).

ACKNOWLEDGMENTS

Funding: Research on polaritons in van der Waals materials is supported as part of Programmable Quantum Materials, an Energy Frontier Research Center funded by the US Department of Energy (DOE), Office of Science, Basic Energy Sciences (BES), under award DE-SC0019443. Work on negative refraction is supported through the Vannevar Bush Faculty Fellow program ONR-VB: N00014-19-1-2630. D.N.B. is a Moore Investigator in Quantum Materials EPIQS GBMF9455. The development of nanophotonics methods is supported by DOE-BES grant DE-SC0018426. Support for the $h^{11}BN$ crystal growth comes from the Office of Naval Research, award N00014-20-1-2474. **Author contributions:** A.J.S. conceived of the study. A.J.S. recorded and analyzed the near-field data, with assistance from S.Z., S.X., S.M., and R.J.; S.M., B.S.Y.K., and S.L. prepared the samples, with guidance from J.H.E., C.D., and J.H.; Y.S. performed far-field measurements. A.R. and M.M.F. performed theoretical calculations, with assistance from A.J.S.; A.J.S., D.N.B., and M.M.F. wrote the manuscript, with input from all the coauthors. **Competing interests:** The authors declare that they have no competing interests. **Data and materials availability:** All data are available in the main text or the supplementary materials.

SUPPLEMENTARY MATERIALS

science.org/doi/10.1126/science.adf1065
Materials and Methods
Supplementary Text
Figs. S1 to S15
Table S1
References (*36*–*45*)

Submitted 30 September 2022; accepted 13 January 2023
10.1126/science.adf1065